

Article

# A Frequency/Phase/Amplitude Estimator for Three-Phase Applications Operating at a Low Sampling Rate

Abdullah M. Abusorrah <sup>1,2</sup>  and Hamed Sepahvand <sup>1,\*</sup> 

<sup>1</sup> Renewable Energy and Power Systems Research Group, King Abdulaziz University, Jeddah 21589, Saudi Arabia; aabusorrah@kau.edu.sa

<sup>2</sup> Department of Electrical and Computer Engineering, Faculty of Engineering, King Abdulaziz University, Jeddah 21589, Saudi Arabia

\* Correspondence: h.sepahvand@ieee.org

**Abstract:** A frequency/phase/amplitude estimator is arguably one of the most crucial components in the control and synchronization of grid-connected equipment. Such an estimator may also be useful for monitoring and protection purposes in power systems. In this paper, an open-loop (and therefore unconditionally stable) estimator for the accurate and rapid extraction of the grid voltage phase, frequency, and amplitude is presented. In designing the proposed technique, special focus is given to applications operating at a low sampling rate. Examples of such applications include high-power converters, where both switching and sampling frequencies are very low. The study concludes with a comprehensive evaluation of the proposed estimator, demonstrating its effectiveness in accurately and swiftly estimating the fundamental parameters of grid voltage under low sampling rates. It highlights the estimator's enhanced performance in scenarios of distorted grid conditions and its superiority in filtering capabilities compared to traditional methods. These findings underline the estimator's potential for broad applicability in power system monitoring, protection, and control.

**Keywords:** amplitude estimation; backward difference formula (BDF); digital signal processing; frequency estimation; fundamental frequency; phase detection; power systems; sampling frequency

MSC: 93B53



**Citation:** Abusorrah, A.M.; Sepahvand, H. A Frequency/Phase/Amplitude Estimator for Three-Phase Applications Operating at a Low Sampling Rate. *Mathematics* **2024**, *12*, 363. <https://doi.org/10.3390/math12030363>

Academic Editor: Xinsong Yang

Received: 19 November 2023

Revised: 15 December 2023

Accepted: 30 December 2023

Published: 23 January 2024



**Copyright:** © 2024 by the authors. Licensee MDPI, Basel, Switzerland. This article is an open access article distributed under the terms and conditions of the Creative Commons Attribution (CC BY) license (<https://creativecommons.org/licenses/by/4.0/>).

## 1. Introduction

Providing an accurate estimation of the grid voltage phase, frequency, and amplitude is extremely important in a wide variety of applications, including distributed generation (DG) systems and microgrids, high-voltage direct current systems, flexible alternating current transmission systems, and power conditioning systems, and in the monitoring and protection of power systems [1–5]. For instance, in DG systems and microgrids, knowledge of the grid phase, frequency, and amplitude is required for a seamless transition from islanding mode to grid-connected mode, as well as for islanding detection [6]. In power systems, accurate frequency detection is crucial for the operation of frequency relays (responsible for over- and under-frequency protection) and for the automatic control of turbines and generators [7].

In recent years, various approaches for estimating grid voltage fundamental parameters have been proposed in the literature. One of the earliest methods was the zero-crossing detection (ZCD)-based technique [8,9]. However, while the ZCD approach is easy to implement, it suffers from two main drawbacks: (1) it often has a poor dynamic response, as the algorithm is updated only every half cycle [10,11]; and (2) its performance deteriorates in the presence of noise, harmonics, and commutation notches, as these disturbances result in multiple zero crossings. Several approaches to improve the performance of the ZCD-based method can be found in later studies [12,13].

An alternative approach for the detection of grid voltage phase, frequency, and amplitude is using the Discrete Fourier Transform (DFT). However, a DFT-based frequency detector requires a high computational effort. This drawback can be alleviated by implementing the DFT method in a recursive form [14]. Nevertheless, some stability concerns regarding the recursive DFT have recently been reported [15].

In a further study [16], an effective frequency estimator is proposed, which is based on a nonlinear Newton-type algorithm and the least-squares method. However, the implementation of this technique demands a very high computational effort. Therefore, to reduce hardware costs, it is implemented at a very low sampling rate.

Phase-locked loop (PLL)-based methods are widely used for extracting the fundamental parameters of grid voltage [17], as they are easy to implement digitally and often offer robust performance. However, special care should be taken in designing and tuning PLLs when they are used for synchronizing grid-connected equipment under weak grid conditions, as the dynamic interaction between the PLL and the converter may result in instability [18]. The methods based on frequency-locked loops (FLLs) are also very popular [19]. Broadly speaking, FLLs are the stationary-reference-frame equivalent of PLLs and, therefore, they share many of the same shortcomings and advantages as PLLs [20].

The aim of this paper is to develop a simple yet efficient method for estimating grid voltage phase, frequency, and amplitude in three-phase applications. The design of the proposed estimator focuses on applications operating at low sampling rates. High-power converters, characterized by low switching and sampling frequencies, exemplify such applications [21,22]. It is important to note that high-power converters are commonly used as the power electronics interface for wind turbines and photovoltaic systems. Their low switching frequency helps in limiting switching losses. Additionally, a frequency estimator with a low sampling rate can be advantageous from an implementation cost perspective. It reduces the need for extensive processing hardware and eliminates the requirement for high-bandwidth sensors [16].

The main contributions of this work are as follows:

- **Open-Loop Nature of the Algorithm:** The proposed algorithm operates in an open-loop manner, ensuring unconditional stability due to the absence of feedback in its control loop. This characteristic is significantly beneficial for synchronizing power converters under weak grid conditions. Moreover, the algorithm does not require tuning control parameters, which is advantageous from an application standpoint. It also provides a rapid dynamic response, crucial for quick post-fault re-tracking capabilities, as demanded by modern grid codes;
- **High Disturbance Rejection Capability:** The algorithm demonstrates an exceptional ability to reject disturbances. In the context of the ever-increasing power quality issues in power systems, this feature is particularly advantageous for synchronization in three-phase applications;
- **Robustness at Low Sampling Rates:** The algorithm exhibits remarkable robustness even at low sampling rates. The analysis and design of synchronization systems at such rates have been largely overlooked in the existing literature, making this aspect of the algorithm particularly noteworthy.

The rest of this work is organized as follows. First, Section 2 provides an overview of the traditional frequency estimation method in three-phase systems and discusses its errors at low sampling frequencies. Then, Section 3 introduces three methods to compensate for frequency errors at low sampling rates. The frequency estimator discussed in Section 2, and consequently, its improved versions in Section 3, rely on access to the fundamental component of the grid voltage. This is challenging because the grid voltage is often heavily contaminated with harmonics and noise. To address this, Section 4 presents the development of an efficient filtering stage based on a chain of delayed signal cancellation operators to extract the grid voltage's fundamental component. Section 5 then discusses how the grid voltage phase and amplitude can be estimated and how the phase and amplitude errors caused by the filtering stage under off-nominal frequencies can be compensated for.

Verification and comparison results are presented in Section 6, and the paper concludes in Section 7.

### 2. Traditional Frequency Estimation Method

A straightforward approach to estimating the grid frequency in three-phase systems involves transferring the three-phase voltages to the stationary ( $\alpha\beta$ ) reference frame by applying the Clarke transformation and calculating the grid frequency as follows:

$$\hat{\omega}_g = \frac{d\left(\tan^{-1}\left(\frac{v_\beta(t)}{v_\alpha(t)}\right)\right)}{dt} = \frac{\dot{v}_\beta(t)v_\alpha(t) - \dot{v}_\alpha(t)v_\beta(t)}{v_\alpha^2(t) + v_\beta^2(t)} \tag{1}$$

As can be observed, the frequency measurement using (1) necessitates the time derivatives of  $v_\alpha$  and  $v_\beta$ , which are most often approximated in the discrete-time domain using a 1-step backward difference formula (BDF1), as follows:

$$\dot{v}_{\alpha\beta}^{1-s}(k) = \frac{v_{\alpha\beta}(k) - v_{\alpha\beta}(k-1)}{T_s} \tag{2}$$

where  $k$  denotes the current sample,  $T_s$  is the sampling time, and the superscript “1 –  $s$ ” indicates the use of the 1-step Backward Difference Formula (BDF1).

Let  $v_\alpha$  and  $v_\beta$  be represented in the discrete-time domain as follows:

$$v_\alpha(k) = V \cos(\omega_g k T_s + \varphi) \tag{3}$$

$$v_\beta(k) = V \sin(\omega_g k T_s + \varphi) \tag{4}$$

where  $V$ ,  $\omega_g$ , and  $\varphi$  represent the amplitude, frequency, and initial phase angle of the grid voltage, respectively. The time derivatives of frequency, amplitude, and initial phase-angle of the grid voltage can be calculated using (2) as follows:

$$\begin{aligned} \dot{v}_\alpha^{1-s}(k) &= \frac{V \cos(\omega_g k T_s + \varphi) - V \cos(\omega_g k T_s + \varphi - T_s \omega_g)}{T_s} \\ &= \frac{V}{T_s} [(1 - \cos(\omega_g T_s)) \cos(\omega_g k T_s + \varphi) - \sin(\omega_g T_s) \sin(\omega_g k T_s + \varphi)] \end{aligned} \tag{5}$$

$$\begin{aligned} \dot{v}_\beta^{1-s}(k) &= \frac{V \sin(\omega_g k T_s + \varphi) - V \sin(\omega_g k T_s + \varphi - T_s \omega_g)}{T_s} \\ &= \frac{V}{T_s} [(1 - \cos(\omega_g T_s)) \sin(\omega_g k T_s + \varphi) + \sin(\omega_g T_s) \cos(\omega_g k T_s + \varphi)]. \end{aligned} \tag{6}$$

By substituting (5) and (6) into (1) and performing some mathematical manipulations, we obtain the following result:

$$\hat{\omega}_g^{1-s} = \frac{\sin(\omega_g T_s)}{T_s} \tag{7}$$

Replacing  $\sin(\omega_g T_s)$  in (7) with its Maclaurin series expansion yields the following:

$$\hat{\omega}_g^{1-s} = \omega_g - \overbrace{\frac{1}{6}(\omega_g^3 T_s^2) + \frac{1}{120}(\omega_g^5 T_s^4) - \frac{1}{5040}\omega_g^7 T_s^6 + \dots}^{\text{error terms}} \tag{8}$$

which clearly indicates a considerable estimation error at low sampling frequencies. In what follows, three approaches to remove this error is presented.

### 3. Frequency Error Correction

#### 3.1. Frequency Error Correction Using Inverse Sine Function

From (7), it can immediately be concluded that the frequency estimation error can be removed by using the inverse sine function (ISF) as

$$\omega_g = \frac{1}{T_s} \sin^{-1} \left( T_s \hat{\omega}_g^{1-s} \right). \tag{9}$$

However, the calculation of the ISF is computationally demanding. Assuming  $\hat{\omega}_g^{1-s} T_s < 1$ , which is often the case, the ISF in (9) can be approximated by the first few terms of its Maclaurin series expansion, as follows:

$$\omega_g = \frac{1}{T_s} \left[ T_s \hat{\omega}_g^{1-s} + \frac{1}{6} \left( T_s \hat{\omega}_g^{1-s} \right)^3 + \frac{3}{40} \left( T_s \hat{\omega}_g^{1-s} \right)^5 + \frac{5}{112} \left( T_s \hat{\omega}_g^{1-s} \right)^7 + \dots \right]. \tag{10}$$

The selection of the number of Maclaurin series terms for the ISF depends on the sampling frequency and involves a tradeoff between detection accuracy and computational effort: a higher number of terms results in lower frequency estimation error, but increases the computational effort. This relationship is clearly illustrated in Figure 1, where ISF $n$  ( $n = 1, 2, 3, 4$ ) represents the consideration of the first  $n$  terms of the ISF Maclaurin series for correcting the frequency estimation error of the traditional method. Notably, ISF1 corresponds to the traditional method without any error compensation. As indicated by the results in Figure 1, considering the first four terms of the ISF Maclaurin series (ISF4) appears to be sufficient for correcting the frequency estimation error at low sampling frequencies.

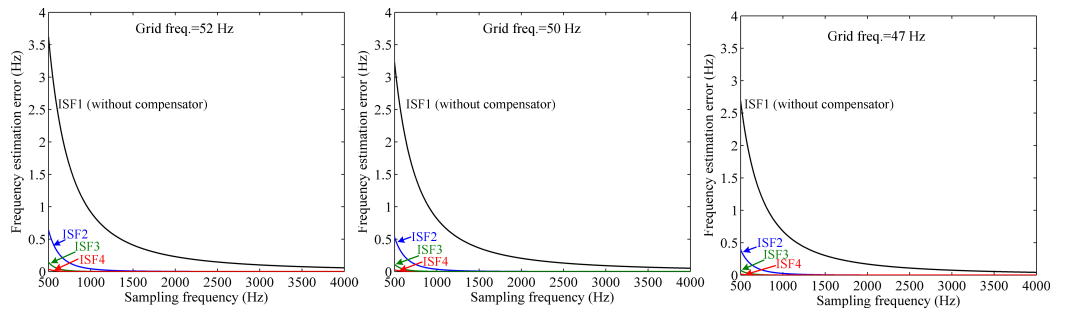


Figure 1. Frequency error correction using the ISF-based method.

#### 3.2. Frequency Error Correction Using a Linear Compensator

Defining  $\omega_g = \omega_n + \Delta\omega_g$ , where  $\omega_n$  is the nominal value of the grid frequency and  $\Delta\omega_n$  denotes the grid frequency deviation from its nominal value, and substituting this into (8) gives

$$\hat{\omega}_g^{1-s} = \omega_n + \Delta\omega_g - \frac{1}{6} (\omega_n + \Delta\omega_g)^3 T_s^2 + \omega_e \tag{11}$$

where  $\omega_e = \frac{1}{120} (\omega_g^5 T_s^4) - \frac{1}{5040} \omega_g^7 T_s^6 + \dots$  is the sum of all but the first error term in (8).

Expanding the third term in the right-hand side of (11) gives

$$\hat{\omega}_g^{1-s} = \omega_n + \Delta\omega_g - \frac{1}{6} \left( \omega_n^3 + 3\omega_n^2 \Delta\omega_g \right) T_s^2 - \underbrace{\frac{1}{6} \left( 3\omega_n \Delta\omega_g^2 + \Delta\omega_g^3 \right) T_s^2}_{\text{negligible}} + \omega_e \tag{12}$$

Using (12) and neglecting the highlighted part,  $\Delta\omega_g, \omega_g$  can be obtained as

$$\Delta\omega_g \approx \frac{\overbrace{1}^{\gamma}}{1 - 0.5\omega_n^2 T_s^2} \left( \hat{\omega}_g^{1-s} - \omega_n + \underbrace{\frac{1}{6}\omega_n^3 T_s^2}_{\psi} \right) \tag{13}$$

$$\omega_g = \Delta\omega_g + \omega_n \approx \gamma \left( \hat{\omega}_g^{1-s} - \omega_n + \psi \right) + \omega_n. \tag{14}$$

Figure 2 shows the schematic of the linear compensator described in (14), and Figure 3 evaluates its performance. As it can be observed, the linear compensator can significantly reduce the frequency estimation error at low sampling frequencies.

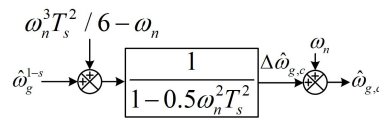


Figure 2. Frequency error compensation using a linear compensator.

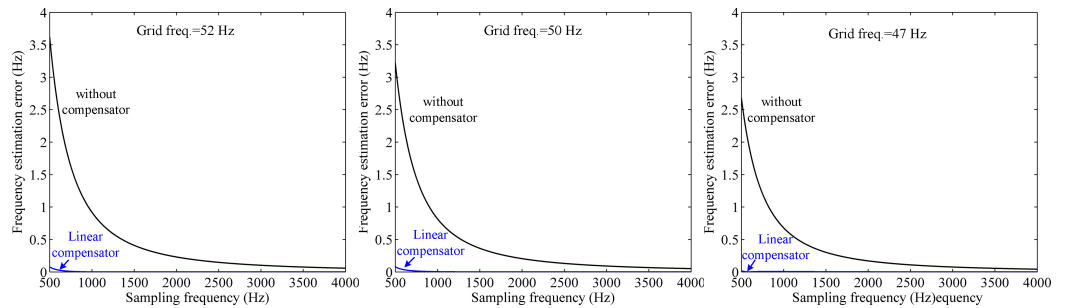


Figure 3. Frequency error correction using a linear compensator.

### 3.3. Frequency Error Correction Using $s$ -Step ( $m \geq 2$ ) BDF

The traditional frequency estimation method, as mentioned earlier, uses the BDF1 (1-step BDF) for the approximation of time derivatives of  $v_\alpha$  and  $v_\beta$ . Therefore, using  $s$ -step ( $s \geq 2$ ) BDF (BDFs) can be a reasonable idea to reduce the estimation error of the traditional method. This section aims to evaluate the effectiveness of this idea for  $s = 2$  to 6. Notice that BDFs with  $s > 6$  are not zero-stable [23] and, therefore, cannot be employed.

Equations (15)–(19) describe the time derivatives of  $v_\alpha$  and  $v_\beta$  using BDFs ( $s = 2$  to 6).

$$\dot{v}_{\alpha\beta}^{2-s}(k) = \frac{3v_{\alpha\beta}(k) - 4v_{\alpha\beta}(k-1) + v_{\alpha\beta}(k-2)}{2T_s} \tag{15}$$

$$\dot{v}_{\alpha\beta}^{3-s}(k) = \frac{11v_{\alpha\beta}(k) - 18v_{\alpha\beta}(k-1) + 9v_{\alpha\beta}(k-2) - 2v_{\alpha\beta}(k-3)}{6T_s} \tag{16}$$

$$\dot{v}_{\alpha\beta}^{4-s}(k) = \frac{25v_{\alpha\beta}(k) - 48v_{\alpha\beta}(k-1) + 36v_{\alpha\beta}(k-2) - 16v_{\alpha\beta}(k-3) + 3v_{\alpha\beta}(k-4)}{12T_s} \tag{17}$$

$$\begin{aligned} \dot{v}_{\alpha\beta}^{5-s}(k) &= \frac{137v_{\alpha\beta}(k) - 300v_{\alpha\beta}(k-1) + 300v_{\alpha\beta}(k-2) - 200v_{\alpha\beta}(k-3)}{60T_s} \\ &+ \frac{75v_{\alpha\beta}(k-4) - 12v_{\alpha\beta}(k-5)}{60T_s} \end{aligned} \tag{18}$$

$$\begin{aligned} \hat{v}_{\alpha\beta}^{6-s}(k) = & \frac{147v_{\alpha\beta}(k) - 360v_{\alpha\beta}(k-1) + 450v_{\alpha\beta}(k-2) - 400v_{\alpha\beta}(k-3)}{60T_s} \\ & + \frac{225v_{\alpha\beta}(k-4) - 72v_{\alpha\beta}(k-5) + 10v_{\alpha\beta}(k-6)}{60T_s} \end{aligned} \quad (19)$$

Using these equations and following the same procedure used for the derivation of (7) gives

$$\hat{\omega}_g^{2-s} = \frac{4 \sin(\omega_g T_s) - \sin(2\omega_g T_s)}{2T_s} \quad (20)$$

$$\hat{\omega}_g^{3-s} = \frac{18 \sin(\omega_g T_s) - 9 \sin(2\omega_g T_s) + 2 \sin(3\omega_g T_s)}{6T_s} \quad (21)$$

$$\hat{\omega}_g^{4-s} = \frac{48 \sin(\omega_g T_s) - 36 \sin(2\omega_g T_s) + 16 \sin(3\omega_g T_s) - 3 \sin(4\omega_g T_s)}{12T_s} \quad (22)$$

$$\hat{\omega}_g^{5-s} = \frac{300 \sin(\omega_g T_s) - 300 \sin(2\omega_g T_s) + 200 \sin(3\omega_g T_s) - 75 \sin(4\omega_g T_s) + 12 \sin(5\omega_g T_s)}{60T_s} \quad (23)$$

$$\begin{aligned} \hat{\omega}_g^{6-s} = & \frac{360 \sin(\omega_g T_s) - 450 \sin(2\omega_g T_s) + 400 \sin(3\omega_g T_s) - 225 \sin(4\omega_g T_s)}{60T_s} \\ & + \frac{72 \sin(5\omega_g T_s) - 10 \sin(6\omega_g T_s)}{60T_s} \end{aligned} \quad (24)$$

Replacing the sine functions in (20) to (24) with their Maclaurin series expansions yields

$$\hat{\omega}_g^{2-s} = \omega_g + \frac{1}{3}\omega_g^3 T_s^2 - \frac{7}{60}\omega_g^5 T_s^4 + \frac{31}{2520}\omega_g^7 T_s^6 + \dots \quad (25)$$

$$\hat{\omega}_g^{3-s} = \omega_g + \frac{3}{10}(\omega_g^5 T_s^4) - \frac{3}{28}(\omega_g^7 T_s^6) + \dots \quad (26)$$

$$\hat{\omega}_g^{4-s} = \omega_g - \frac{1}{5}(\omega_g^5 T_s^4) + \frac{13}{42}(\omega_g^7 T_s^6) - \dots \quad (27)$$

$$\hat{\omega}_g^{5-s} = \omega_g - \frac{5}{14}(\omega_g^7 T_s^6) + \dots \quad (28)$$

$$\hat{\omega}_g^{6-s} = \omega_g + \frac{1}{7}(\omega_g^7 T_s^6) + \dots \quad (29)$$

Comparing (25) with (8) indicates that the BDF2 increases the frequency estimation error. Therefore, it should not be used. However, the other BDFs, particularly BDF6, reduce the frequency estimation error. This fact can be clearly observed in Figure 4.

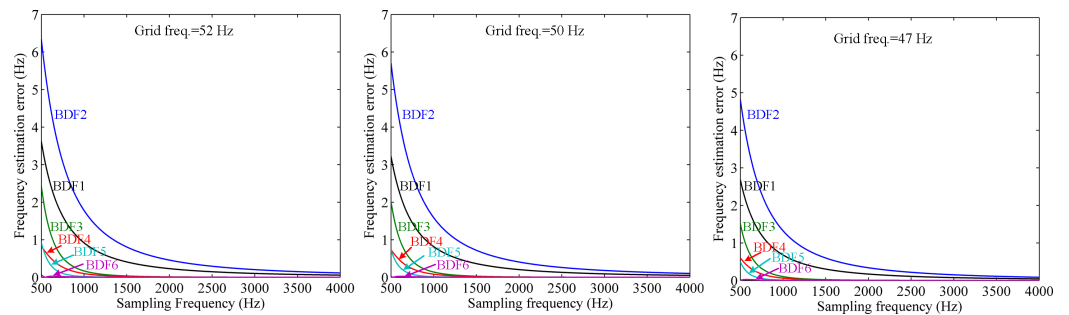


Figure 4. Frequency error correction using different BDFs.

#### 4. Filtering of the Grid Voltage Disturbance Components

The presence of dc offset, harmonics, and the fundamental frequency negative sequence (FFNS) component in the grid voltage results in an error in the estimation of grid frequency using (1). Therefore, the  $\alpha\beta$ -axis voltage components should be filtered out before using them in the calculation of grid frequency. To achieve this goal, the  $\alpha\beta$ -frame delayed signal cancelation ( $\alpha\beta$ DSC) operator is employed in this paper. Equation (30) describes this operator in the  $z$ -domain [24,25], in which  $n$  is called the delay factor and  $N_n = (T/n)/T_s$  ( $T$  is nominal value of the grid fundamental period)

$$\alpha\beta\text{DSC}_n(z) = \frac{1}{2} \left[ 1 + e^{\frac{j2\pi}{n}} z^{-N_n} \right]. \tag{30}$$

In the  $z$ -domain definition of  $\alpha\beta$ DSC operator, it is assumed that  $N_n$  is an integer. This assumption, however, may not be always true as the sampling frequency may be determined by factors other than the  $\alpha\beta$ DSC operator. In such scenario, the fractional delay can be approximated by interpolation techniques as [26]

$$\alpha\beta\text{DSC}_n(z) = \frac{1}{2} \left[ 1 + e^{\frac{j2\pi}{n}} z^{-N_{n,i}} \left( 1 - N_{n,f} + N_{n,f} z^{-1} \right) \right] \tag{31}$$

where  $N_{n,i} = \text{floor}(N_n)$  and  $N_{n,f} = N_n - N_{n,i}$ .

Based on its delay factor, each  $\alpha\beta$ DSC operator can block certain harmonics. Therefore, to deal with real grid scenarios, cascading multiple  $\alpha\beta$ DSC operators with appropriate delay factors is often required. Table 1 summarizes different combinations of  $\alpha\beta$ DSC operators for various grid scenarios and Figure 5 shows their Bode magnitude plots. Notice that  $\alpha\beta\text{CDSC}_{n_1, n_2, \dots, n_m}$  operator denotes the cascade connection of  $m$   $\alpha\beta$ DSC operators with delay factors  $n_1, n_2, \dots, n_m$ . It should be emphasized here that all these combinations have the  $\alpha\beta\text{DSC}_4$  operator in common and, therefore, all of them can block the FFNS component of the grid voltage.

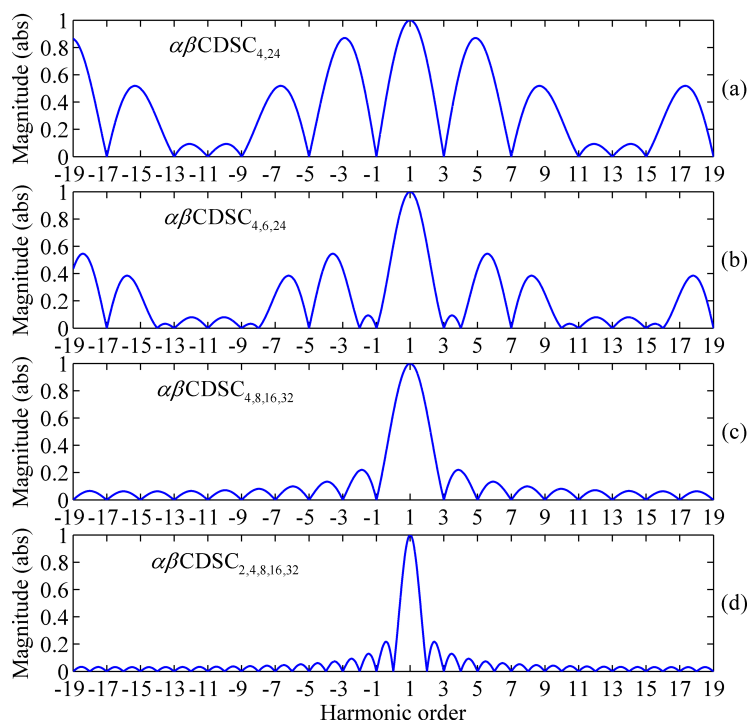


**Figure 5.** Bode magnitude plot of (a)  $\alpha\beta\text{CDSC}_{4,24}$  operator, (b)  $\alpha\beta\text{CDSC}_{4,6,24}$  operator, (c)  $\alpha\beta\text{CDSC}_{4,8,16,32}$  operator, and (d)  $\alpha\beta\text{CDSC}_{2,4,8,16,32}$  operator.

**Table 1.** Different Scenarios for the Grid Harmonic Pattern and Proper Combination of  $\alpha\beta$ DSC Operators to Deal with Them.

|         | Grid Harmonic Pattern   | Proper $\alpha\beta$ CDSC                 |
|---------|---|---|
| Known   | non-triplen odd harmonics of order $-5, +7, -11, +13, -17, +19$ | $\alpha\beta$ CDSC <sub>4,24</sub>        |
|         | symmetrical   | $\alpha\beta$ CDSC <sub>4,6,24</sub>      |
|         | odd harmonic components   | $\alpha\beta$ CDSC <sub>4,8,16,32</sub>   |
|         | asymmetrical  | $\alpha\beta$ CDSC <sub>2,4,8,16,32</sub> |
| Unknown | -   |   |

In addition to the grid harmonic pattern, a special attention should be paid to the Nyquist rate, which is half of the sampling rate, in selecting the proper combination of  $\alpha\beta$ DSC operators. For example, if the sampling frequency is 1.2 kHz (the Nyquist rate is 600 Hz) and the grid harmonic pattern is asymmetrical, then using the  $\alpha\beta$ DSC<sub>32</sub> operator in the combination of  $\alpha\beta$ DSC operators recommended in Table 1, i.e., the  $\alpha\beta$ CDSC<sub>2,4,8,16,32</sub> operator, is useless. The reason is that the lowest harmonic frequency that the  $\alpha\beta$ DSC<sub>32</sub> operator can block is  $-750$  Hz (the negative sign denotes a negative sequence harmonic frequency), which is beyond the Nyquist rate (In this paper, it is assumed that the sampling frequency has been carefully chosen based on the grid harmonic content and antialiasing filter capability in the attenuation of harmonics. In other words, it is presumed that harmonic components with frequencies beyond the Nyquist rate are very negligible or have been canceled out before the A/D conversion using the antialiasing filter. Therefore, there is no need to be worry about the aliasing problems caused by finite sampling).

The  $\alpha\beta$ CDSC operator, regardless of its components, provides a zero gain at its targeted harmonic frequencies when the grid frequency is at its nominal value. In the presence of frequency drifts, however, it is not able to do so. To deal with this problem, the  $\alpha\beta$ CDSC operator can be adapted to the grid frequency variations, but at the cost of a much higher computational effort and implementation complexity [27]. An alternative approach is the repeated passes of the signal through the identical  $\alpha\beta$ CDSC operator. To better visualize this, Figure 6 compares the Bode magnitude plots of a single  $\alpha\beta$ CDSC<sub>2,4,8,16,32</sub> operator and two series-connected  $\alpha\beta$ CDSC<sub>2,4,8,16,32</sub> operators. It is immediately clear that series-connected  $\alpha\beta$ CDSC<sub>2,4,8,16,32</sub> operators provide a much higher filtering capability. This improvement, however, is at the cost of doubling the transient time. Therefore, selecting the number of series-connected  $\alpha\beta$ CDSC operators involves a tradeoff between speed of response and filtering capability.

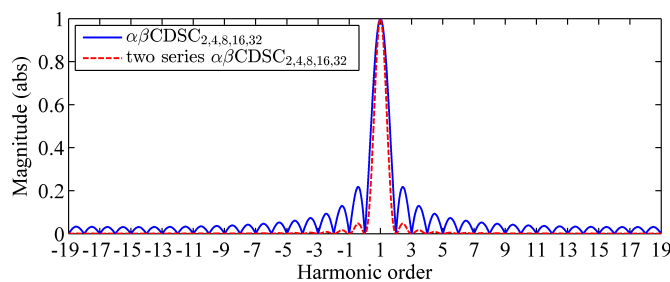


**Figure 6.** Bode magnitude plots of a single  $\alpha\beta$ CDSC<sub>2,4,8,16,32</sub> operator and two series-connected  $\alpha\beta$ CDSC<sub>2,4,8,16,32</sub> operators.

### 5. Phase and Amplitude Estimation

The prefiltering stage ( $\alpha\beta$ CDSC operator) provides an accurate estimation of the fundamental frequency positive-sequence (FFPS) component when the grid frequency is at its nominal value. In this condition, the grid voltage phase and amplitude can be easily and effectively estimated using

$$\hat{\theta}_1^+ = \tan^{-1} \left( \frac{\hat{\vartheta}_{\beta,1}^+}{\hat{\vartheta}_{\alpha,1}^+} \right) \tag{32}$$

$$\hat{V}_1^+ = \sqrt{(\hat{\vartheta}_{\alpha,1}^+)^2 + (\hat{\vartheta}_{\beta,1}^+)^2} \tag{33}$$

where  $\hat{\vartheta}_{\alpha,1}^+$  and  $\hat{\vartheta}_{\beta,1}^+$  are outputs of the prefiltering stage. These expressions, however, cannot provide an accurate estimation of phase and amplitude in the presence of frequency drifts, because the FFPS component extracted by the  $\alpha\beta$ CDSC operator undergoes a phase-shift and amplitude scaling in this condition. Fortunately, as an estimation of grid frequency is available, these errors can be corrected by modifying (32) and (33) as

$$\hat{\theta}_{1,c}^+ = \tan^{-1} \left( \frac{\hat{\vartheta}_{\beta,1}^+}{\hat{\vartheta}_{\alpha,1}^+} \right) - \hat{\theta}_c^+ \tag{34}$$

$$\hat{V}_{1,c}^+ = \frac{\sqrt{(\hat{\vartheta}_{\alpha,1}^+)^2 + (\hat{\vartheta}_{\beta,1}^+)^2}}{\hat{V}_c^+} \tag{35}$$

where  $\hat{\theta}_c^+$  and  $\hat{V}_c^+$  are estimations for the phase and amplitude of the  $\alpha\beta$ CDSC operator at the fundamental frequency of positive-sequence, respectively. In what follows, compact expressions for  $\theta_c^+$  and  $V_c^+$  are derived.

As mentioned in the previous section, the prefiltering stage ( $\alpha\beta$ CDSC operator) may be composed of two or more  $\alpha\beta$ DSC operators with appropriate delay factors. It was also pointed out that a higher filtering capability under off-nominal grid frequencies can be achieved through the series connection of identical  $\alpha\beta$ CDSC operators. Therefore, in general form, the prefiltering stage z-domain transfer function can be expressed as

$$G(z) = [\alpha\beta\text{CDSC}_{n_1, n_2, \dots, n_m}(z)]^p = [\alpha\beta\text{DSC}_{n_1}(z)]^p \times [\alpha\beta\text{DSC}_{n_2}(z)]^p \times \dots \times [\alpha\beta\text{DSC}_{n_m}(z)]^p \tag{36}$$

where  $p$  is the number of identical  $\alpha\beta$ CDSC operators.

Substituting  $z = e^{j\omega_g T_s}$  in (36) and performing some mathematical simplifications gives the phase and amplitude of the prefiltering stage at the fundamental frequency as

$$\theta_c^+ = \angle G(e^{j\omega_g T_s}) = - \overbrace{\frac{pT}{2} \left[ \frac{1}{n_1} + \frac{1}{n_2} + \dots + \frac{1}{n_m} \right]}^{k_\varphi} \Delta\omega_g \tag{37}$$

$$V_c^+ = \left| G(e^{j\omega_g T_s}) \right| \approx 1 - \underbrace{\frac{pT^2}{8} \left[ \frac{1}{n_1^2} + \frac{1}{n_2^2} + \dots + \frac{1}{n_m^2} \right]}_{k_v} \Delta\omega_g^2 \tag{38}$$

where  $\Delta\omega_g = \omega_g - \omega_n$ , as defined before, is the deviation of the grid frequency from its nominal value.

### 6. Real-Time Simulation Results

To verify the effectiveness of the proposed estimators, some real-time simulation tests using the dSPACE 1006 platform were conducted, and their results are presented in this section. To provide flexibility in conducting tests, the three-phase input signals are generated internally in dSPACE. Using the dSPACE Control Desk, the obtained results are recorded, and then plotted in the Matlab environment.

#### 6.1. Comparison between Different Versions of the Proposed Estimator

Figures 7–9 show all three versions of the proposed estimator. Each of these structures has the same prefiltering stage (i.e., two series-connected  $\alpha\beta$ CDSC<sub>2,4,8,16</sub> operators) and

identical phase/amplitude detectors. The only difference between them is their frequency detector, which affects their overall performance. Note that the estimated frequency is a key element in phase/amplitude error compensators. For the sake of brevity, the structure shown in Figure 7, which uses BDF1 for the approximation of derivative functions and considers the first four terms of the Maclaurin series (10) to correct frequency estimation errors, is referred to as Estimator1. The structure depicted in Figure 8, similar to Estimator1, employs BDF1 for the approximation of derivative functions but uses a linear frequency error compensator, and is referred to as Estimator2. The third version, depicted in Figure 9, is called Estimator3. This estimator, as shown, uses BDF6 for the implementation of derivative functions. In the evaluation studies, the sampling frequency is considered to be 800 Hz. The gains of the phase and amplitude error compensators can be easily calculated according to (37) and (38), considering the selected prefiltering stage as  $k\varphi = 3/160$  and  $k_v = 85/2,560,000$ .

To evaluate the performance of the proposed estimators, four test cases are designed:

- Test Case 1: A step change of  $+40^\circ$  occurs in the grid voltage phase angle;
- Test Case 2: A step change of  $+2$  Hz occurs in the grid voltage frequency;
- Test Case 3: The grid voltage is harmonically distorted. In this test, the grid voltage components are  $V_1^+ = 1$  pu,  $V_5^- = 0.06$  pu, and  $V_7^+ = 0.05$  pu, resulting in a total harmonic distortion of approximately 7.8%. The grid frequency is fixed at  $+47$  Hz during this test. This test is conducted under off-nominal grid frequency because the prefiltering stage completely blocks harmonics when the grid frequency is at its nominal value;
- Test Case 4: An exaggeratedly large (0.5 pu) DC component is added to the “A” phase of the grid voltage. As in the previous test, the grid frequency is  $+47$  Hz during this test.

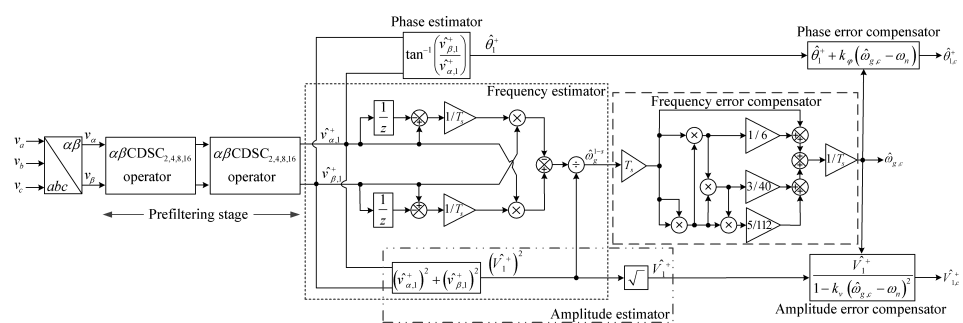


Figure 7. First version of the proposed estimator, which is referred to as Estimator1.

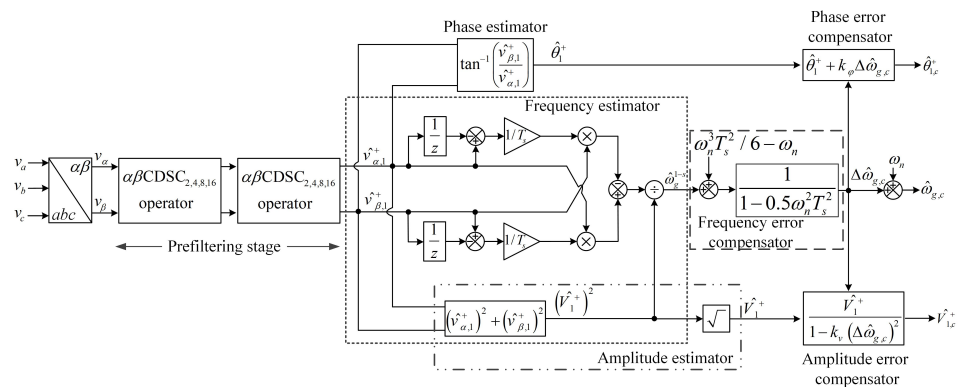


Figure 8. Second version of the proposed estimator, which is referred to as Estimator2.

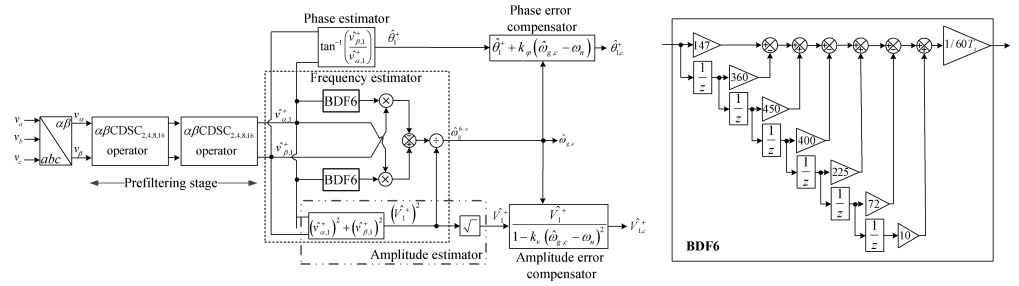


Figure 9. Third version of the proposed estimator, which is referred to as Estimator3.

Figures 10 and 11 show the obtained results for Test Cases 1 and 2, respectively. It can be observed that all estimators, particularly Estimator1, provide good steady-state detection accuracy. From the perspective of dynamic response, all three versions exhibit similar performance and reach steady-state after approximately two cycles of the nominal frequency.

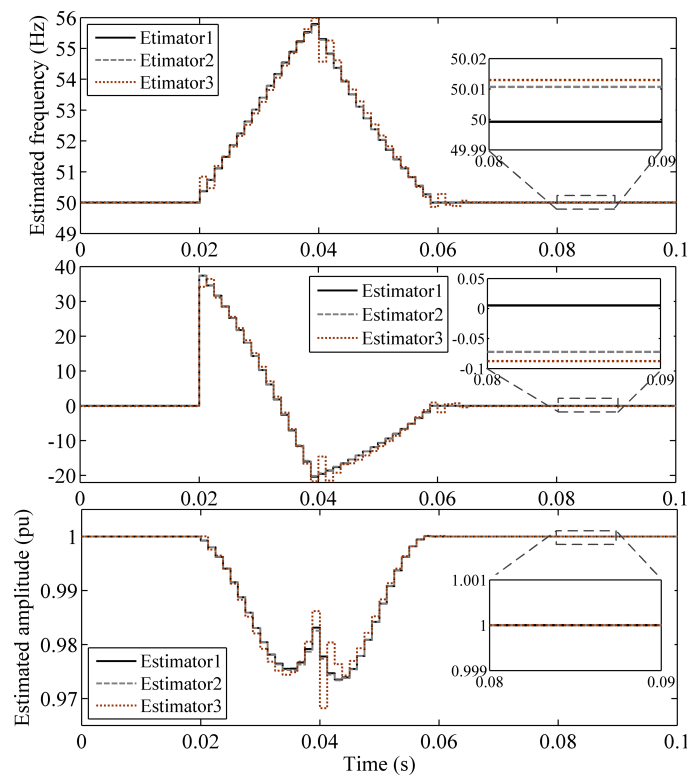


Figure 10. Obtained results under test case 1.

Figure 12 presents the results obtained under Test Case 3. As shown, Estimator1 and Estimator2 demonstrate significantly better performance than Estimator3. The reason is that Estimator3 uses BDF6 for the approximation of derivative functions, and this method, as seen in Figure 13, leads to much higher noise and harmonic amplification compared to BDF1.

Figure 14 displays the results under Test Case 4. Thanks to the action of the prefiltering stage, which completely blocks the DC component, all estimators, particularly Estimator1, demonstrate good performance in this test.

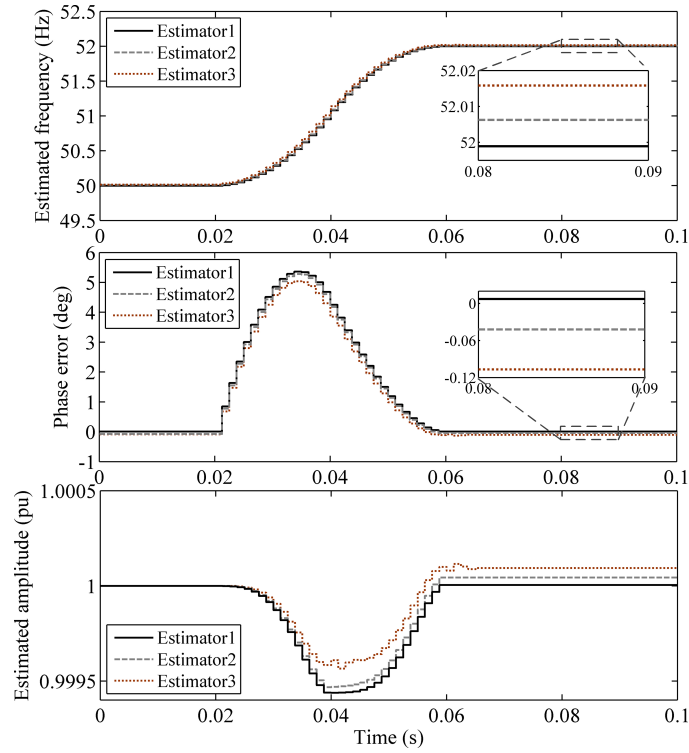


Figure 11. Obtained results under test case 2.

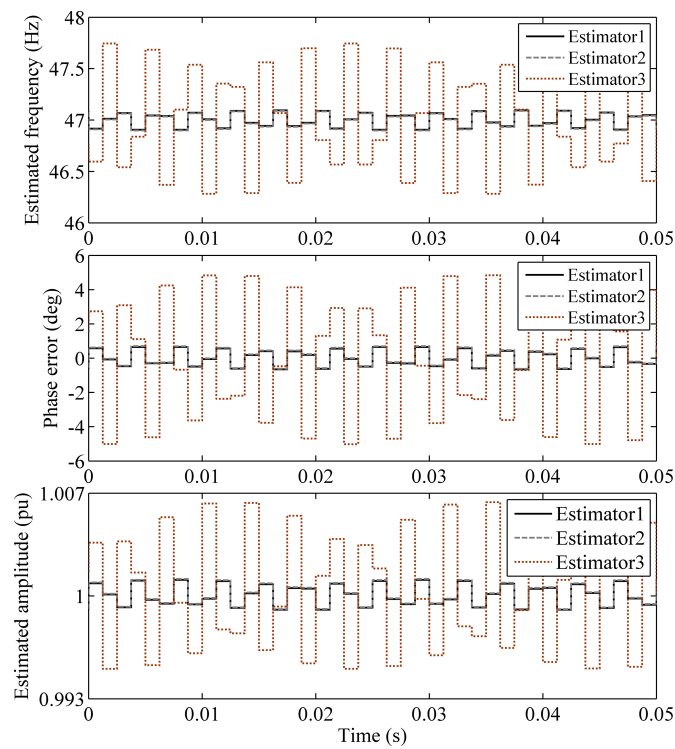
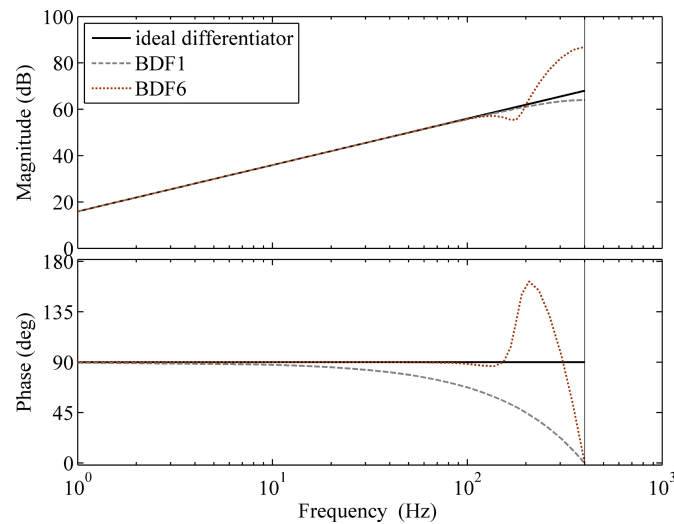
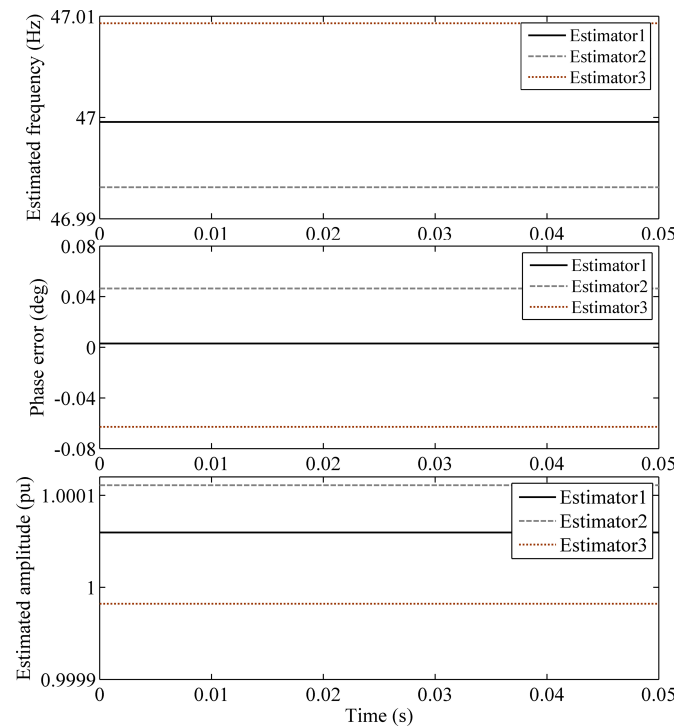


Figure 12. Obtained results under test case 3.



**Figure 13.** Frequency response of the BDF1-based and BDF6-based approximate differentiators and the ideal (continuous) differentiator.



**Figure 14.** Obtained results under test case 4.

### 6.2. Comparison with a Standard FLL

In the previous section, it was demonstrated that Estimator1 outperforms its variants. This section will present a performance comparison between Estimator1 and a Reduced-Order Generalized-Integrator-based Frequency-Locked Loop (ROGI-FLL), a standard synchronization tool in three-phase applications [28]. The block diagram implementation of ROGI-FLL is illustrated in Figure 15. The control parameters of the ROGI-FLL are set to  $k = 190$  and  $\lambda = 8900$  based on the guidelines provided in [29]. Three tests will be conducted:

- Test Case A: The grid voltage is initially clean and free of noise or disturbances. Then, a 5% DC component is suddenly introduced to Phase A of the grid voltage;

- Test Case B: The grid voltage is in a balanced condition. Suddenly, a double-line-to-ground fault occurs;
- Test Case C: The grid voltage is distorted with harmonics of orders  $-5$  and  $+7$ ;
- Test Case D: The grid voltage undergoes a ramping change in the grid frequency at  $20 \text{ Hz/s}$  for a duration of  $0.1 \text{ s}$ .

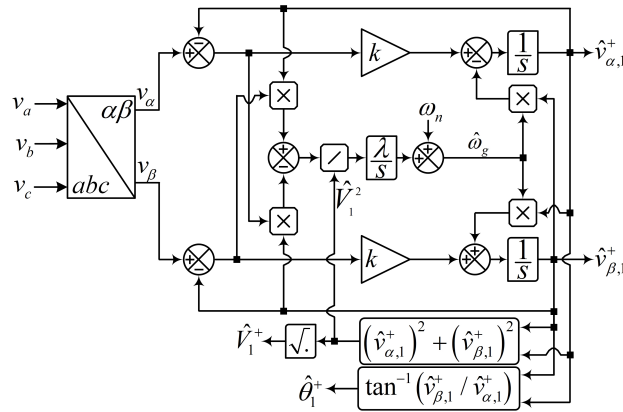


Figure 15. ROGI-FLL.

The results of the above tests are shown in Figures 16–19. Based on these results, the following observations can be made:

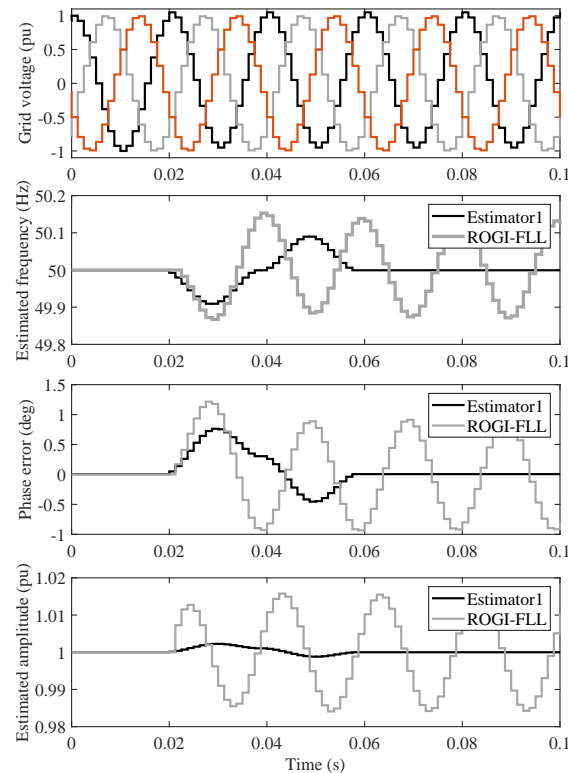
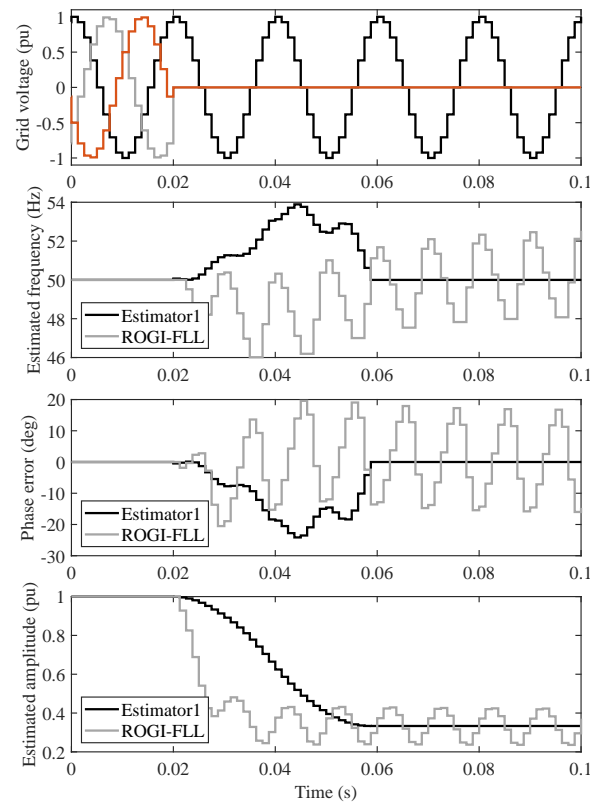
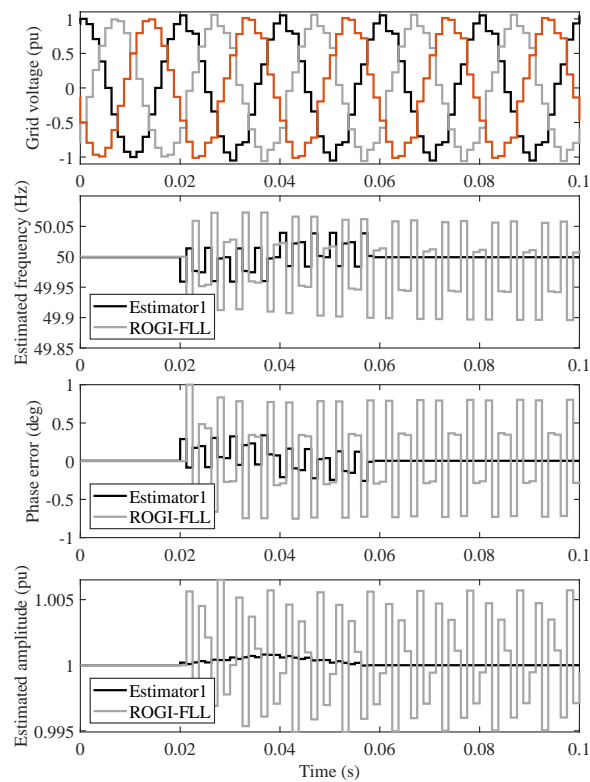


Figure 16. Test Case A Results: Performance analysis of Estimator1 and ROGI-FLL during a sudden addition of 5% DC component to phase A of clean grid voltage.



**Figure 17.** Test Case B Results: Comparative response of Estimator1 and ROGI-FLL to a double-line-to-ground fault in a balanced grid voltage condition.



**Figure 18.** Test Case C Results: Comparative response of Estimator1 and ROGI-FLL in handling harmonics of orders  $-5$  and  $+7$  in the grid voltage.

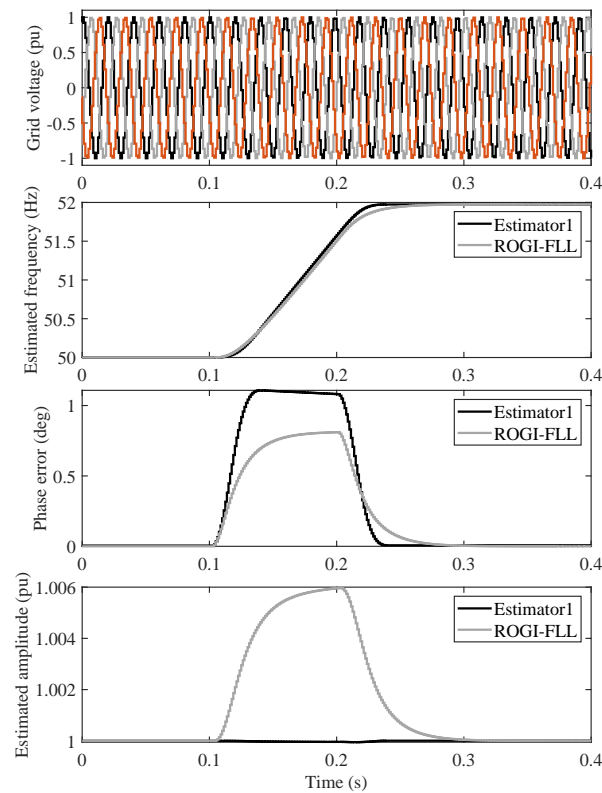


**Figure 19.** Test Case D Results: Comparative response of Estimator1 and ROGI-FLL in handling a frequency ramping change.

- Estimator1 effectively filters the DC component. However, ROGI-FLL suffers from large fundamental-frequency oscillatory ripples in the presence of a DC component (see Figure 16);
- Estimator1 effectively handles unbalanced grid scenarios with a fast dynamic response. However, ROGI-FLL suffers from large double-frequency oscillatory errors under this condition (see Figure 17);
- Estimator1 effectively filters dominant harmonics of orders  $-5$  and  $+7$ . In contrast, ROGI-FLL suffers from large harmonics at six times the fundamental frequency in this condition (see Figure 18);
- Both Estimator1 and ROGI-FLL have a phase offset error during the frequency ramping interval. This error is slightly larger for Estimator1 compared to ROGI-FLL. In contrast, the estimated amplitude of Estimator1, unlike ROGI-FLL, has no offset error during the frequency ramping interval, and the estimated frequency of Estimator1 converges to the final value faster (see Figure 19).

## 7. Summary and Conclusions

The aim of this paper was to develop a simple estimator for accurately and quickly estimating the fundamental parameters of grid voltage, namely frequency, phase, and amplitude, for applications operating at a low sampling rate. The study began with an analysis of the traditional frequency detection method. It was demonstrated that this method results in considerable estimation error under low sampling frequencies. To rectify this error, three approaches were proposed: The first and second methods involved adding a compensator to the output of the traditional frequency detection method, while the last relied on using a high-order backward difference method for approximating derivative functions. It was then discussed that the traditional frequency estimation approach, which is fundamental to the proposed frequency estimator, is highly sensitive to grid voltage harmonics and noise; therefore, these elements should be removed before the grid voltage

is input into the frequency estimator. The use of the  $\alpha\beta$ CDSC operator was proposed for this purpose, and its design aspects for different grid scenarios were discussed in detail. It was subsequently shown that the phase and amplitude of the grid voltage can be effectively extracted using the outputs of the  $\alpha\beta$ CDSC operator and the frequency estimated by the proposed frequency detector. All three versions of the proposed estimator were then evaluated under various test cases. The results showed that, unlike the first and second versions of the proposed estimator, the third version (which uses BDF6 for approximating derivative functions) has poor disturbance rejection capability and therefore may not be suitable for distorted grid conditions. It should be noted that all three versions of the proposed estimator exhibit comparable dynamic behavior.

Additionally, a critical comparison between Estimator1 and the ROGI-FLL was conducted. Estimator1 showed superior performance in filtering out DC components, handling unbalanced grid scenarios, and filtering dominant harmonics. In contrast, ROGI-FLL faced challenges with oscillatory errors under similar conditions. This comparison highlighted the strengths of Estimator1 compared to a traditional estimator.

A limitation of Estimator1 and its variants, Estimator2 and Estimator3, which may not be immediately clear, is the requirement for storing a considerably higher number of samples compared to traditional methods, like the ROGI-FLL. This situation becomes more severe if the delay lengths are not divisible by the sampling period. In such cases, interpolation techniques need to be adopted to approximate fractional delays, which increases the memory requirement. This could pose a challenge in the low-cost implementation of control algorithms using low-cost microprocessors, particularly considering that the phase/frequency/amplitude estimator is just one element within several other control loops required for controlling power converters.

**Author Contributions:** Conceptualization, A.M.A. and H.S.; methodology, A.M.A. and H.S.; software, H.S.; validation, A.M.A. and H.S.; formal analysis, H.S.; investigation, A.M.A.; resources, A.M.A.; writing—original draft preparation, A.M.A. and H.S.; writing—review and editing, A.M.A. and H.S.; visualization, A.M.A. and H.S.; supervision, A.M.A.; project administration, A.M.A.; funding acquisition, A.M.A. All authors have read and agreed to the published version of the manuscript.

**Funding:** This research work was funded by Institutional Fund Projects under grant no. (IFPIP: 1202-135-1443). The authors gratefully acknowledge technical and financial support provided by the Ministry of Education and King Abdulaziz University (KAU), DSR, Jeddah, Saudi Arabia.

**Data Availability Statement:** Data are contained within the article.

**Conflicts of Interest:** The authors declare no conflict of interest.

## References

- Smadi, I.A.; Atawi, I.E.; Ibrahim, A.A. An Improved Delayed Signal Cancellation for Three-Phase Grid Synchronization with DC Offset Immunity. *Energies* **2023**, *16*, 2873. [\[CrossRef\]](#)
- Zhao, D.; Wang, F.; Li, S.; Zhao, W.; Chen, L.; Huang, S.; Wang, S.; Li, H. An Optimization of Least-Square Harmonic Phasor Estimators in Presence of Multi-Interference and Harmonic Frequency Variance. *Energies* **2023**, *16*, 3397. [\[CrossRef\]](#)
- Zhang, Q.; Xu, Y.; Wang, X.; Yu, Z.; Deng, T. Real-Time Wind Field Estimation and Pitot Tube Calibration Using an Extended Kalman Filter. *Mathematics* **2021**, *9*, 646. [\[CrossRef\]](#)
- Ullah, F.U.M.; Khan, N.; Hussain, T.; Lee, M.Y.; Baik, S.W. Diving Deep into Short-Term Electricity Load Forecasting: Comparative Analysis and a Novel Framework. *Mathematics* **2021**, *9*, 611. [\[CrossRef\]](#)
- Bizon, N.; Thounthong, P. A Simple and Safe Strategy for Improving the Fuel Economy of a Fuel Cell Vehicle. *Mathematics* **2021**, *9*, 604. [\[CrossRef\]](#)
- Hmad, J.; Houari, A.; Bouzid, A.E.M.; Saim, A.; Trabelsi, H. A Review on Mode Transition Strategies between Grid-Connected and Standalone Operation of Voltage Source Inverters-Based Microgrids. *Energies* **2023**, *16*, 5062. [\[CrossRef\]](#)
- Bindi, M.; Piccirilli, M.C.; Luchetta, A.; Grasso, F. A Comprehensive Review of Fault Diagnosis and Prognosis Techniques in High Voltage and Medium Voltage Electrical Power Lines. *Energies* **2023**, *16*, 7317. [\[CrossRef\]](#)
- Friedman, V. A zero crossing algorithm for the estimation of the frequency of a single sinusoid in white noise. *IEEE Trans. Signal Process.* **1994**, *42*, 1565–1569. [\[CrossRef\]](#)
- Pauluk, M.; Piątek, P.; Baranowski, J. Efficient Zero-Value-Cross Detection for Single-Phase Mains-Powered Motors: A Comparative Study. *Energies* **2023**, *16*, 6298. [\[CrossRef\]](#)

10. Wang, Y.F.; Li, Y.W. An overview of grid fundamental and harmonic components detection techniques. In Proceedings of the IEEE ECCE 2013, Denver, CO, USA, 15–19 September 2013; p. 51855192.
11. Ciobotaru, M. Reliable Grid Condition Detection and Control of Single Phase Distributed Power Generation Systems. Ph.D. Thesis, Aalborg University, Aalborg, Denmark, 2009.
12. Duric, M.B.; Durisic, Z.R. Frequency measurement in power networks in the presence of harmonics using Fourier and zero crossing technique. In Proceedings of the Power Tech 2005, St. Petersburg, Russia, 27–30 June 2005; pp. 1–6.
13. Vainio, O.; Ovaska, S.J.; Polla, M. Adaptive filtering using multiplicative general parameters for zero-crossing detection. *IEEE Trans. Ind. Electron.* **2003**, *50*, 1340–1342. [[CrossRef](#)]
14. Sozanski, K.; Szczesniak, P. Advanced Control Algorithm for Three-Phase Shunt Active Power Filter Using Sliding DFT. *Energies* **2023**, *16*, 1453. [[CrossRef](#)]
15. Darwish, H.A.; Fikri, M. Practical considerations for recursive DFT implementation in numerical relays. *IEEE Trans. Power Deliv.* **2007**, *22*, 42–49. [[CrossRef](#)]
16. Sadinezhad, I.; Agelidis, V.G. Slow sampling online optimization approach to estimate power system frequency. *IEEE Trans. Smart Grid* **2011**, *2*, 265–277. [[CrossRef](#)]
17. Martin-Martinez, S.; Gomez-Lazaro, E.; Molina-Garcia, A.; Fuentes, J.A.; Viguera-Rodriguez, A.; Plata, S.A. A new three-phase DPLL frequency estimator based on nonlinear weighted mean for power system disturbances. *IEEE Trans. Power Deliv.* **2013**, *28*, 179–187. [[CrossRef](#)]
18. Dong, D.; Wen, B.; Boroyevich, D.; Mattavelli, P.; Xue, Y. Analysis of phase-locked loop low-frequency stability in three-phase grid-connected power converters considering impedance interactions. *IEEE Trans. Ind. Electron.* **2015**, *62*, 310–321. [[CrossRef](#)]
19. Rodriguez, P.; Luna, A.; Etxeberria, I.; Teodorescu, R.; Blaabjerg, F. A stationary reference frame grid synchronization system for three-phase grid-connected power converters under adverse grid conditions. *IEEE Trans. Power Electron.* **2012**, *27*, 99–112. [[CrossRef](#)]
20. Ghartemani, M.K.; Khajehoddin, S.A.; Jain, P.K.; Bakhshai, A. Problems of startup and phase jumps in PLL systems. *IEEE Trans. Power Electron.* **2012**, *27*, 1830–1838. [[CrossRef](#)]
21. Yim, J.-S.; Sul, S.-K.; Bae, B.-H.; Patel, N.R.; Hiti, S. Modified current control schemes for high-performance permanent-magnet AC drives with low sampling to operating frequency ratio. *IEEE Trans. Ind. Appl.* **2009**, *45*, 763–771. [[CrossRef](#)]
22. Freijedo, F.D.; Vidal, A.; Yepes, A.; Guerrero, J.; Lopez, O.; Malvar, J.; Doval-Gandoy, J. Tuning of synchronous-frame PI current controllers in grid-connected converters operating at a low sampling rate by MIMO root locus. *IEEE Trans. Ind. Electron.* **2015**, *62*, 5006–5017. [[CrossRef](#)]
23. Suli, E.; Mayers, D.F. *An Introduction to Numerical Analysis*; Cambridge University Press: Cambridge, UK, 2003.
24. Wang, Y.F.; Li, Y.W. Grid synchronization PLL based on cascaded delayed signal cancellation. *IEEE Trans. Power Electron.* **2011**, *26*, 1987–1997. [[CrossRef](#)]
25. Wang, Y.F.; Li, Y.W. Analysis and digital implementation of cascaded delayed-signal-cancellation PLL. *IEEE Trans. Power Electron.* **2011**, *26*, 1067–1080. [[CrossRef](#)]
26. Laakso, T.I.; Valimaki, V.; Karjalainen, M.; Laine, U.K. Splitting the unit delay. *IEEE Signal Process. Mag.* **1996**, *13*, 30–60. [[CrossRef](#)]
27. Golestan, S.; Freijedo, F.D.; Vidal, A.; Yepes, A.G.; Guerrero, J.M.; Doval-Gandoy, J. An efficient implementation of generalized delayed signal cancellation PLL. *IEEE Trans. Power Electron.* **2015**, *31*, 1085–1094. [[CrossRef](#)]
28. Golestan, S.; Guerrero, J.M.; Vasquez, J.C.; Abusorrah, A.M.; Al-Turki, Y. Linear Time-Periodic Modeling, Examination, and Performance Enhancement of Grid Synchronization Systems With DC Component Rejection/Estimation Capability. *IEEE Trans. Power Electron.* **2021**, *36*, 4237–4253. [[CrossRef](#)]
29. Golestan, S.; Guerrero, J.M.; Vasquez, J.C.; Abusorrah, A.M.; Al-Turki, Y. A Study on Three-Phase FLLs. *IEEE Trans. Power Electron.* **2019**, *34*, 213–224. [[CrossRef](#)]

**Disclaimer/Publisher’s Note:** The statements, opinions and data contained in all publications are solely those of the individual author(s) and contributor(s) and not of MDPI and/or the editor(s). MDPI and/or the editor(s) disclaim responsibility for any injury to people or property resulting from any ideas, methods, instructions or products referred to in the content.